Multi-objective Optimization for Rapid Identification of Novel Compound Metals for Interconnect Applications

Akash Ramdas, Guanyu Zhou, Yansong Li, Ping-Lien Lu, Evan R. Antoniuk, Evan J. Reed, Christopher L. Hinkle, Felipe H. da Jornada**

Abstract

Interconnect materials play the critical role of routing energy and information in integrated circuits. However, established bulk conductors, such as copper, perform poorly when scaled down beyond 10 nm, limiting the scalability of logic devices. Here, we develop a multi-objective search, combined with first-principles calculations, to rapidly screen over 15,000 materials and discover new interconnect candidates. Our approach simultaneously optimizes the bulk electronic conductivity, surface scattering time, and chemical stability using physically motivated surrogate properties accessible from materials databases. We identify promising local interconnects that have the potential to outperform ruthenium, the current state-of-the-art post-Cu material, and also semi-global interconnects with potentially large skin depths at the GHz operation frequency. We validate our approach on one of the identified candidates, CoPt, using both *ab-initio* and experimental transport studies, showcasing its potential to supplant Ru and Cu for future local interconnects.

Akash Ramdas
Department of Materials Science and Engineering, Stanford University, Stanford, CA 94305, USA
Email Address: akashr@stanford.edu
Guanyu Zhou
Department of Electrical Engineering, University of Notre Dame, Notre Dame, IN 46556, USA
Yansong Li
Department of Electrical Engineering, University of Notre Dame, Notre Dame, IN 46556, USA
Ping-Lien Lu
Department of Electrical Engineering, University of Notre Dame, Notre Dame, IN 46556, USA
Evan R. Antoniuk
Department of Chemistry, Stanford University, Stanford, CA 94305, USA
Evan J Reed
Department of Materials Science and Engineering, Stanford University, Stanford, CA 94305, USA
Christopher L. Hinkle
Department of Electrical Engineering, University of Notre Dame, Notre Dame, IN 46556, USA
Felipe H. da Jornada
Department of Materials Science and Engineering, Stanford University, Stanford, CA 94305, USA
Email Address: jornada@stanford.edu

Keywords: *Interconnects, Copper Alternatives, Multi-Objective, mm-Wave, Materials Discovery*

1 Introduction

Interconnects act as the transportation network of integrated circuits. As the logic components of these circuits become smaller, it is essential to have interconnects that possess desirable properties at the concomitant smaller length scales. In fact, the International Roadmap for Devices and Systems (IRDS)'s 2021 More Moore update identifies: "The most difficult challenge for interconnects is the introduction of new materials that meet the wire conductivity requirements, reduce dielectric permittivity, and meet reliability requirements." [1] Due to Cu's rapid decrease in electrical conductivity at smaller length scales caused by increased surface and grain boundary scattering [2, 3], there has been considerable efforts in identifying alternative metals for interconnect applications. Contemporary studies searching for such alternative interconnect materials tend to use one of the following approaches: 1) identifying materials that show a *smaller decrease* in conductivity upon reducing the metal thickness [4, 5, 6]; 2) searching for materials displaying novel physics (such as non-trivial topology, etc.), which effectively leads to an increase in the conductivity upon reducing their thickness [7, 5, 8, 9, 10]; and 3) revisiting, experimentally, varied well-established materials ranging from elemental metals [11, 12], silicides [13], intermetallic aluminides [14, 15, 16], and even carbon nanotubes [17]. The first approach typically optimizes only for a single property – the conductivity's scalability –, which could lead to candidate materials that are difficult to integrate into devices or have lower bulk conductivity values. The second approach, which focuses on materials hosting unusual physics, is promising; however, the transport mechanisms of such materials are not fully understood even from a fundamental perspective, resulting in a longer period of time before they can be widely adopted in devices. The third approach involves the systematic study of a large number of materials whose electrical conductivities were not accurately determined in high-quality samples. It is arguably the preferred method of validating individual candidates, but it relies heavily on experiments and is therefore impractical to be carried out for all but a small number of hand-picked materials.

In this work, we develop a computational screening approach to identify promising interconnect materials to ensure the experimental efforts focus on the most promising material systems. To design such a screen-

ing effort, one must first identify multiple figures of merit of interconnect materials. Aside from the bulk conductivity and the decrease in conductivity due to surface scattering, identifying a liner-free and barrier-free interconnect candidate can greatly improve a candidate's viability. Liners and barriers are needed to prevent electromigration and reactions with the surrounding low-k dielectric, atmospheric water, and oxygen molecules. However, these layers, such as the current standard interconnect barrier layer, TaN, consumes precious nanometers of space in the interconnect. In fact, the replacement of TaN with alternative 2D materials is a currently evolving research area [18]. This is extermely critical to address for local interconnects, with a pitch of 1-20 nm. Identifying new metals that may not need a barrier is challenging because these stability properties are difficult to estimate from a theoretical perspective and have been mostly determined using focused experimental studies [19, 20].

An additional merit of this work comes from the application to semi-global interconnects (pitch of 0.1-50 μm) for mm-wave/GHz frequency applications. This is particularly pressing given that Cu displays a low skin depth of about 10 μm at such GHz frequencies, decreasing the effective conduction cross-section for high-frequency applications. Such a low skin depth further limits the applicability of Cu for semi-globa interconnects further from the complementary metal-oxide semiconducting (CMOS) elements. Laminate stacks containing a ferromagnetic material and Cu have been proposed as a way to enhance skin depth while retaining Cu's promising conductivity [21]. These stacks combine the ferromagnet's negative permeability and copper's high conductivity to enhance Cu's skin depth at particular frequencies[22]. More broadly, however, it would be desirable to identify materials that natively show high conductivity and skin depth as alternatives to the proposed laminates [21, 22] for such applications.

The ideal post-Cu interconnect should meet multiple requirements to perform at an appropriate level for commercialization. The intertwined nature of the requirements led us to develop a multi-objective optimization approach to identify candidate systems. But while common, multi-objective methods for materials selection have found limited applicability for the discovery of novel interconnect materials. That can be partially attributed to the challenge of co-optimizing for various materials properties, some of which (*e.g.*, the bulk conductivity and surface scattering time) are anti-correlated, as we detail in section 2.2. For instance, constraint-based filtering is quite common for materials discovery [23, 24, 25, 26, 27, 28], but requires a fine-tuning of the various filters for anti-correlated properties. We avoid this issue by working on the Pareto fronts and identifying classes of materials that are nearly optimal given a set of desired figures of merit.

To complement the above-mentioned previous efforts and expand the search space of materials for interconnects, we design a rapid, generalizable, and physics-informed method to screen a large number of material candidates. We use the space of materials curated computationally by the Materials Project database [29, 30, 31] as a starting point for our screening efforts. We focus on the materials in the Materials Project database that have a corresponding inorganic crystal structure database (ICSD) entry, *i.e.*, they have been previously synthesized. This allows our identified candidates to be readily made by following existing synthesis steps reported in the literature.

In this work, we develop an integrated approach identifying relevant figures of merit desired in interconnect materials and their associated *surrogate properties* readily available in computational materials databases (Figure 1). The main result of our work, detailed in section 2, is the list of the most promising local (Figure 3) and semi-global (Figure 4) interconnects. To further validate our approach, we also present an in-depth study of one of the top candidates from our search, CoPt. In section 2.4, we report *ab initio* transport calculations based on density-functional perturbation theory (DFPT), indicating that high-quality CoPt crystals should display a bulk conductivity comparable to that of Cu. In addition, in section 2.5, we report experimental transport measurements on CoPt, thin films from previous literature, strongly suggesting that CoPt indeed displays a better resistance to surface scattering than Cu when thinned down to less than 10 nm. In addition we also experimentally demonstrate the remarkable air stability of grown CoPt films, in section 2.5. Taken together, our results demonstrate not only the promise of CoPt as a future interconnect material but, more broadly, the potential of our multi-objective search approach based on physically motivated and computationally accessible surrogate properties. We anticipate that the tens of potential materials we identify here to be prioritized in future experimental study of novel interconnects.

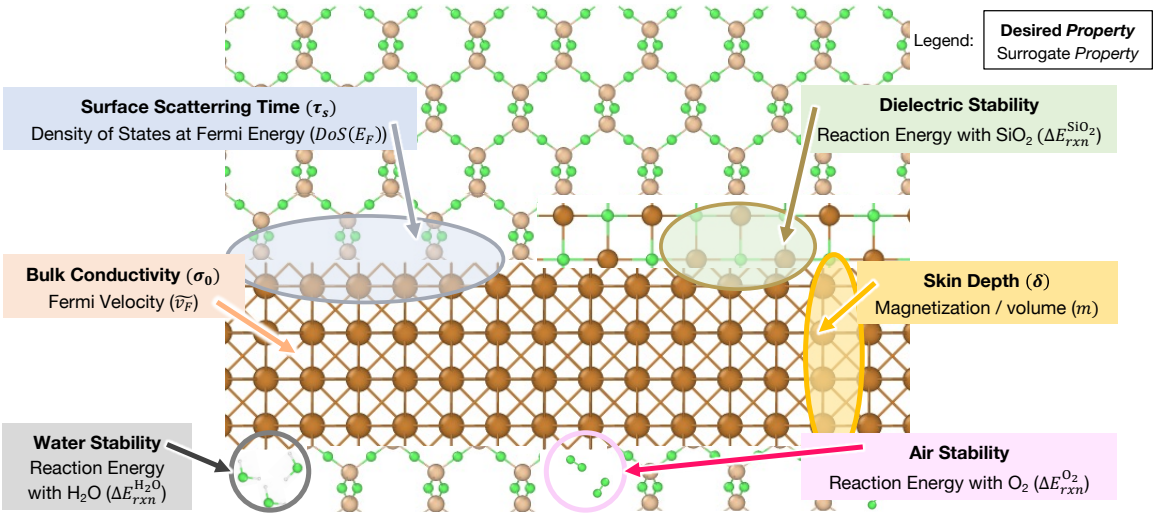

Figure 1: A schematic representation of an interconnect and its surrounding environment. Indicated on the schematic are properties that are screened for in this work. Under the properties, we list the corresponding surrogate properties, that we use to screen for these properties.

2 Results and Discussion

2.1 Obtaining surrogate properties

Our work starts by identifying relevant figures of merit that should be optimized for interconnects, which we take as the bulk conductivity, surface scattering time, dielectric stability, air stability, water stability, and skin depth. However, such figures of merit cannot be rapidly computed for a diverse group of chemical formulas. We hence identify surrogate properties readily available in computational materials databases which we expect to correlate with these figures of merit. The figures of merit and the surrogate properties we identify are shown schematically in Figure 1. To filter for compounds that are stable and synthesizable, we take the energy of the compound with respect to the convex hull as a filter [32], computed as the energy difference between the material and the most stable phase at the same composition computed using density-functional theory (DFT) calculations. In the following sections, we describe the approximations we use to identify all surrogate properties for the desired physical quantity. We emphasize that, while these surrogate properties are rough approximations of the desired physical properties, they are still useful in filtering the wide space of materials and selecting candidates for follow-up *ab initio* calculations and experimental validation efforts. We obtain all surrogate properties from the Materials Project database for 17,033 previously synthesized metals. This dataset acts as a starting point for our screening to identify the best candidate interconnect materials. We summarize the properties and their surrogate properties in Table 1.

2.1.1 Fermi velocity as a surrogate property for the bulk conductivity

The bulk conductivity tensor of a crystalline metal $\sigma(T)$ can be written within the self-energy relaxation time approximation as [33]

$$\sigma_{\alpha\beta}(T) = -\frac{e^2}{\Omega}\sum_n \int_{\mathrm{BZ}} \frac{d\mathbf{k}}{\Omega_{\mathrm{BZ}}} \mathbf{v}^{\alpha}_{n\mathbf{k}} \mathbf{v}^{\beta}_{n\mathbf{k}} \frac{\partial f^0_{n\mathbf{k}}}{\partial \varepsilon_{n\mathbf{k}}} \tau_{n\mathbf{k}}, \quad (1)$$

where the subscript indices α, β denote Cartesian components, T is temperature, Ω is the unit cell volume, Ω_{BZ} is the Brillouin zone (BZ) volume, $\mathbf{v}^{\alpha}_{n\mathbf{k}}$ denotes the velocity of the band n at reciprocal lattice vector $\mathbf{k}$ within the BZ along the Cartesian direction α, $f^{(0)}_{n\mathbf{k}}$ is the Fermi-Dirac distribution function for the equilibrium electronic population at temperature T, and τ_{nk} is the electron scattering time for state $|n\mathbf{k}\rangle$. We focus on the zero-temperature limit of this quantity,

$$\sigma_{\alpha\beta}(T \to 0) = \frac{e^2}{\Omega}\sum_n \int_{\mathrm{FS}} \frac{d\mathbf{k}}{\Omega_{\mathrm{BZ}}} \mathbf{v}^{\alpha}_{n\mathbf{k}} \mathbf{v}^{\beta}_{n\mathbf{k}} \frac{1}{|\mathbf{v}_{n\mathbf{k}}|} \tau_{n\mathbf{k}}, \quad (2)$$

which only depends on states $|n\mathbf{k}\rangle$ lying on the Fermi surface (FS), which has an area we denote by A_{FS}.

We focus on the trace of the conductivity tensor,

$$\sigma_0 \equiv \sum_{\alpha} \sigma_{\alpha\alpha} = \frac{e^2}{\Omega}\sum_n \int_{\mathrm{FS}} \frac{d\mathbf{k}}{\Omega_{\mathrm{BZ}}} |\mathbf{v}_{n\mathbf{k}}| \tau_{n\mathbf{k}}. \quad (3)$$

The most computationally demanding quantity to evaluate Equation 3 is the electron scattering time τ_{nk}, which, for high-quality bulk materials at low temperatures, is dictated by scattering with phonons. We denote

Relevant Physical Property	Surrogate Property
Bulk Conductivity (σ_0)	Band structure Fermi velocity ($\tilde{v}_F$)
Surface Scattering Time (τ_s)	Density of states at the Fermi level ($D(E_F)$)
Skin Depth (δ)	Magnetization per unit volume (m)
Air Stability	Thermodynamic 0K reaction energy with O_2($\Delta E^{rxn}_{O_2}$)
Water Stability	Thermodynamic 0K reaction energy with H_2O($\Delta E^{rxn}_{H_2O}$)
Dielectric Stability	Thermodynamic 0K reaction energy with SiO_2($\Delta E^{rxn}_{SiO_2}$)
Thermal Stability	Energy above the convex hull ($E_{\text{above hull}}$)

Table 1: Summary of all properties and the corresponding identified surrogates

by $g_{mn\nu}(\mathbf{k},\mathbf{q})$ the electron-phonon coupling matrix element between an initial electronic state $|n\mathbf{k}\rangle$ and a final state $|m\mathbf{k}+\mathbf{q}\rangle$ due to the interaction with a phonon with branch index ν and wavevector $\mathbf{q}$, one can write

$$\begin{aligned}\tau^{-1}_{n\mathbf{k}} = \frac{2\pi}{\hbar}\sum_{m,\nu}\int \frac{d\mathbf{q}}{\Omega_{\text{BZ}}}|g_{mn\nu}(\mathbf{k},\mathbf{q})|^2\times \\ [(n_{\mathbf{q}\nu}+1-f^0_{m\mathbf{k}+\mathbf{q}})\delta(\varepsilon_{nk}-\varepsilon_{m\mathbf{k}+\mathbf{q}}-\hbar\omega_{\mathbf{q}\nu}) \\ +(n_{\mathbf{q}\nu}+f^0_{m\mathbf{k}+\mathbf{q}})\delta(\varepsilon_{nk}-\varepsilon_{m\mathbf{k}+\mathbf{q}}+\hbar\omega_{\mathbf{q}\nu})].\end{aligned} \tag{4}$$

We are interested in the scattering times for states close to the Fermi surface; hence, we obtain that $\tau^{-1}_{n\mathbf{k}} \propto \langle g\rangle_{\text{FS}} D(\varepsilon_F)$, where $D(\varepsilon_F)$ is the density of states at the Fermi level ε_F, and $\langle g\rangle_{\text{FS}}$ is an average of the electron-phonon coupling matrix elements $g_{mn\nu}(\mathbf{k},\mathbf{q})$ over the relevant states $|m\mathbf{k}+\mathbf{q}\rangle$ close to the Fermi surface. To first order, ignoring the materials' specific dependence on $\langle g\rangle_{\text{FS}}$, we approximate that $\tau^{-1}_{n\mathbf{k}} \propto D(\varepsilon_F)$. Putting this back in Equation 3 we obtain

$$\begin{aligned}\sigma_0 &= \frac{e^2}{\Omega}\frac{1}{D(\varepsilon_F)}\sum_n\int_{\text{FS}} d\mathbf{k}|\mathbf{v}_{n\mathbf{k}}| \\ &\approx \frac{e^2}{\Omega\Omega_{\text{BZ}}}(A_{FS})\langle|\mathbf{v}|\rangle_{\text{FS}},\end{aligned} \tag{5}$$

where $\langle|\mathbf{v}|\rangle_{\text{FS}}$ denotes the Fermi velocity averages over the Fermi surface. Since $D(\varepsilon_F)$ can be written as $A_F\langle\frac{1}{|\mathbf{v}|}\rangle_{\text{FS}}$, and applying the fact that $\frac{1}{\langle\frac{1}{|\mathbf{v}|}\rangle_{\text{FS}}}$ is less than $\langle|\mathbf{v}|\rangle_{\text{FS}}$, we obtain

$$\sigma_0 \propto \frac{1}{\langle\frac{1}{|\mathbf{v}|}\rangle_{\text{FS}}}\langle|\mathbf{v}|\rangle_{\text{FS}} \sim \langle|\mathbf{v}|\rangle^2_{\text{FS}}. \tag{6}$$

Hence, the conductivity increases with $\langle v\rangle_{\text{FS}}$, as expected from our intuition. The question is how to quickly estimate $\langle v\rangle_{\text{FS}}$ for a large set of materials.

While materials databases such as the Materials Project [29] provide a rich set of total energy and band structure calculations, the regular k-point grids on which such calculations are performed on the whole BZ are too coarse for accurate estimates of the Fermi surface-averaged band velocities. We also found that interpolation methods based solely on energies and not the Kohn-Sham wavefunctions, such as Fourier-based interpolation methods [34], are inaccurate due to band crossings [35]. As a practical solution, we approximate the average velocity $\langle v\rangle_{\text{FS}}$ using estimates taken from the one-dimensional paths on which the electronic band structure was evaluated in the Materials Project database [30], which we denote by $\tilde{v}_F$. *We hence take $\tilde{v}_F$ as our surrogate property for bulk conductivity,* $\sigma_0 \propto \tilde{v}_F$. To compute this quantity for each material we take the finite diference slope at all $\mathbf{k}$ points in the band structure close (0.02 eV) to the Fermi level. We take an average of all these Fermi level crossing velocities to obtain $\tilde{v}_F$.

2.1.2 Fermi level density of states as a surrogate property for the surface scattering time

To obtain a surrogate for the surface scattering times, we base our analysis on the Fuchs-Sondheimer and Mayadas-Shatzkes models [2, 3]. The Fuchs-Sondheimer model allows one to incorporate the effects of surfaces by modeling the resistivity of the material in terms of its bulk resistivity (ρ_0), bulk mean free path (λ_0), surface specularity and film geometry. The effect of grain boundaries can be accounted for within the Mayadas-Shatzkes model, for instance, which ascribes a grain-boundary contribution to the resistivity in terms of the bulk resistivity, bulk mean free path, grain size, and reflection coefficient. Both these models allow one to approximate the resistivity of a material, $\rho(d)$ in terms of the bulk resistivity and the increase in resistivity due to defect scattering (here surface and grain boundaries), ρ_{s+gb} as $\rho(d) = \rho_0 + \rho_{s+gb} = \rho_0 + \rho_0\lambda_0\tilde{\Gamma}$, where $\tilde{\Gamma}$ captures both the geometry of the metal film and the internal grain boundary parameters. However, we expect the grain boundary contribution to to be quite sensitive to the synthesis and materials processing conditions. Hence we expect the quantity $\rho_0\lambda_0$, and therefore its surrogate metric, to better capture the surface scattering than the grain boundary scattering.

Accordingly, in this work, we focus on the thickness-dependent resistivity of a material from the standpoint of the Fuchs-Sondheimer model. In this case we have $\rho(d) = \rho_0 + \rho_s = \rho_0 + \rho_0\lambda_0\Gamma(d)$, where $\rho(d)$ is the resistivity at some thickness d, ρ_s is the surface contribution to the resistivity (inversely proportional to the surface scattering time τ_s), and Γ is some geometric function of the film thickness d. The surface contribution to the resistivity can be determined from first principles using [4]

$$\frac{1}{\rho_0\lambda_0} = \sum_n \int_{\text{BZ}} \frac{e^2}{2\pi^3} d\mathbf{k} \frac{\partial f^0_{n\mathbf{k}}}{\partial \varepsilon_{n\mathbf{k}}} \frac{(\mathbf{v}_{nk} \cdot \hat{j})^2}{|v_{nk}|}, \quad (7)$$

where n are the relevant band indices, BZ is the Brillouin zone, f^0 denotes the Fermi-Dirac distribution of a Bloch state $|n\mathbf{k}\rangle$ with an energy $\varepsilon_{n\mathbf{k}}$. To obtain further insights, we restrict this to the 0K temperature limit and assume that the electron velocity is always along the current direction $\hat{j}$, for which we obtain that $\frac{1}{\rho_0\lambda_0} \propto \sum_n \int_{FS} d\mathbf{k} \propto A_{FS}$. We know that $A_{\text{FS}} = \frac{D(\varepsilon_F)}{\langle \frac{1}{|\mathbf{v}|} \rangle_{\text{FS}}} \sim D(\varepsilon_F)\langle |\mathbf{v}| \rangle_{\text{FS}}$. The reduction in surface scattering relaxation time τ_s (or increase in the scattering rate due to the surface) is responsible for this increased resistivity. Hence, the surface relaxation time τ_s is inversely proportional to the increase in resistivity $\rho(d) - \rho_0$. Since we are already maximizing $\langle |\mathbf{v}| \rangle_{\text{FS}}$ in our previous surrogate, we take the $D(\varepsilon_F)$ as the surrogate property for the surface scattering time, which should be maximized. To compute this quantity we fit a spline to the density of states obtainined from Materials Project and interpolate it's value to the Fermi level.

2.1.3 Volume magnetization as a surrogate property for the skin depth

The resistance R of an interconnect at an external time-varying electric field with frequency ω is determined by the effective area available for electrical conduction, $A_{\text{eff}}(\omega)$. This is in general lower than the physical area of the interconnect material due to the presence of eddy currents, resulting in a finite skin depth for the material. This is critical for semi-global interconnects where the size of the interconnect becomes larger than the skin depth at high frequencies. This leads to the resistance being determined by the skin depth $\delta(\omega)$ and the bulk conductivity σ_0 of the material, $R \propto \frac{1}{\sigma_0\delta(\omega)}$. At high frequencies, the impedance Z of a material is given by [36]

$$Z(\omega) = R_0 \frac{a}{2\delta_0(\omega)} [\sqrt{\mu_R(\omega)} - j\sqrt{\mu_L(\omega)}], \quad (8)$$

where R_0 is the DC electrical resistance, μ_R and μ_L denote the resistive and inductive contributions of the permeability, and δ_0 is the non-magnetic skin depth. δ_0 can be written in terms of the bulk resistivity ρ_0 as $\delta_0 = \sqrt{\frac{2\rho_0}{\omega}}$.We can write $\mu_R = |\mu_t| + \mu''_t$, and $\mu_L = |\mu_t| - \mu''_t$, where $\mu_t = \mu'_t - j\mu''_t$ is the complex circumferential permeability. To minimize the absolute impedance at a given high frequency for a given wire dimension, one has to minimize $\sqrt{\rho(\mu_L + \mu_R)}$. This can be achieved by looking for highly conductive ferromagnetic metals, with a tunable permeability. This tunability is present near the anti-resonance and resonance frequency. The ferromagnetic resonant frequency is proportional to the square root saturation magnetization of the material [37]. To have materials showing this favorable behavior at high frequency, we need a high value of saturation magnetization (M_s). We capture this by the magnetization per unit volume obtained from DFT calculations, which we denote by m, and which we take as the surrogate property for the skin depth.This property is readily available as a computed metric from the Materials Project database.

2.1.4 Thermodynamic reaction energies as surrogate properties for the environmental stability

Reactivity, activation energies, and dynamic properties are quite difficult to obtain for a wide variety of materials. To simplify our analysis, we hence take the thermodynamic reaction enthalpy at 0K as the surrogate property to estimate this complex quantity. Accordingly, we expect thermodynamically stable interconnects (*i.e.*, displaying a non-negative reaction enthalpy) to have a low likelihood of reacting with surrounding compounds and substrates. This simplification however cannot predict the formation of a passive product layer (usually oxide), that can prevent further reaction. If a surrogate property to avoid this limitation is found, one can further expand the space of viable candidates.

We compute the relevant reaction enthalpies by constructing the convex hull of the experimentally observed compounds from the Materials Project database and finding the most stable product. [32, 38]. For example, for the reaction betwee Ag and SiO_2, we would construct the Ag-Si-O phase diagram and identify the decomposition products on Ag + SiO_2 tie-line. We consider the reaction with the environmental molecules (water, oxygen) and the surrounding dielectric (SiO_2) as the main reaction energies we would like to optimize. We denote these surrogate properties by ΔE_z^{rxn} where we consider z to be either O_2, H_2O, or SiO_2.

2.2 Analysis of the computed surrogate properties

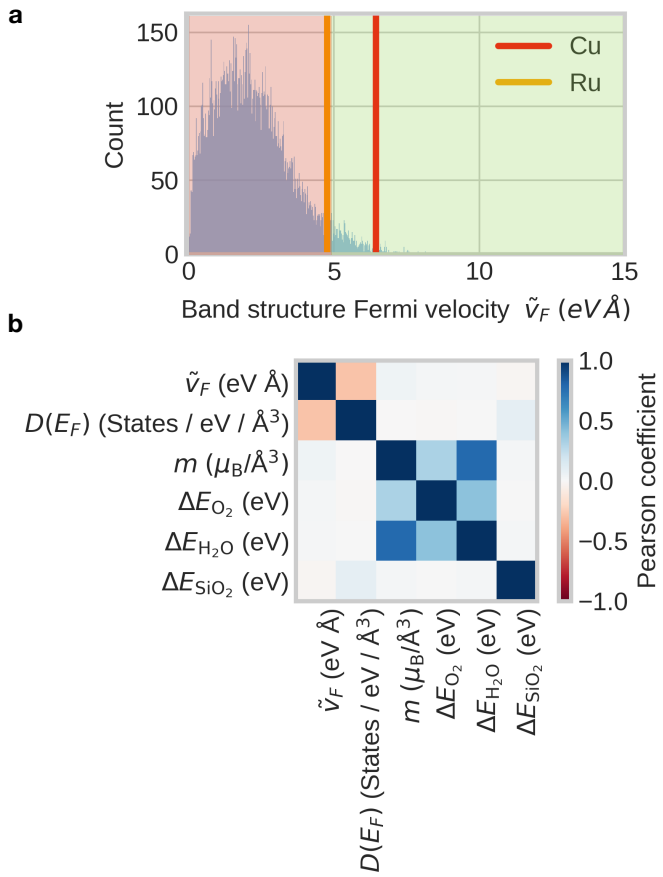

Figure 2: a) Histogram of the Fermi velocity distribution of the surveyed materials, highlighting the difficulty in finding a better conductor than Cu (red vertical line) and even Ru (yellow vertical line). b) Correlation matrix showing the interdependence of the computed surrogate properties used to identify potential interconnect materials, highlighting the need for a multiobjective approach. Symbols are defined in Table 1.

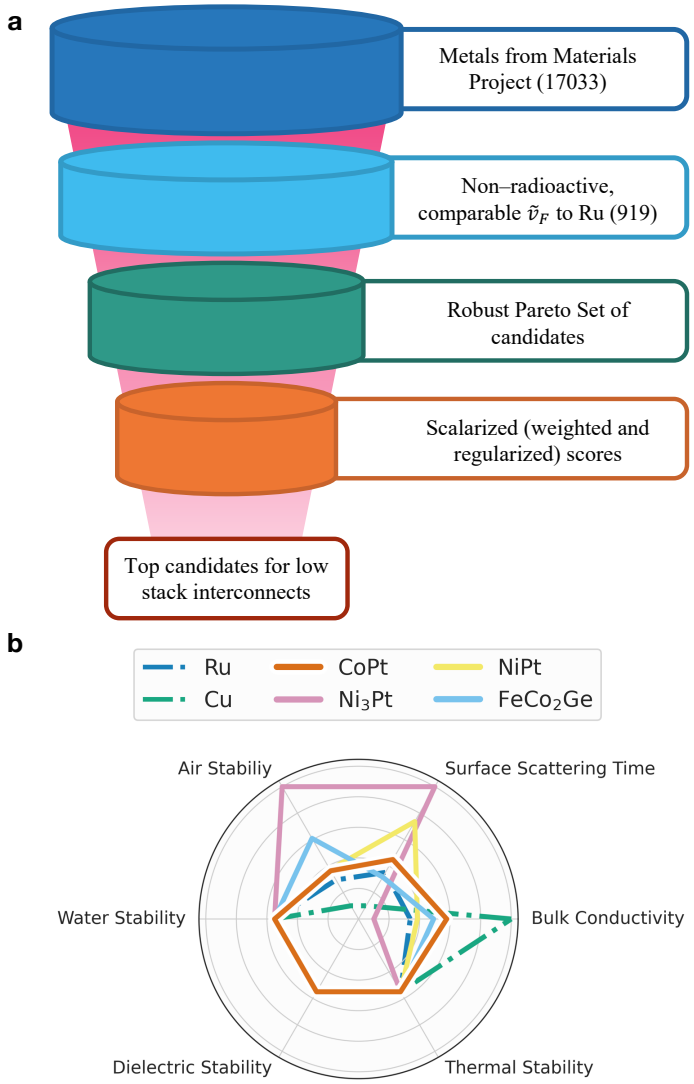

Figure 3: a) Procedure for identification of local interconnects. b) Scaled radar plot, normalized by the maximum value associated with each of the surveyed surrogate properties, for the identified local interconnect candidates from the screening (solid) and the current state-of-the-art alternatives (dotted).

In Figure 2, we report the distribution of the Fermi velocities obtained from our screened candidates, from which it becomes evident that only very few materials display a band-structure-averaged Fermi velocity $\tilde{v}_F$ larger than that of established interconnect materials such as Cu or Ru. This suggests that few materials can outperform them in their bulk conductivities, and that identifying a Cu replacement for local interconnects will involve finding a material that holistically displays the set of properties highlighted in Figure 1. In Figure 2, we also show the correlations between all the surrogate properties. We highlight the weak anti-correlation between the surface scattering time and bulk conductivity surrogates. This showcases the intertwined nature of our problem space. This further demonstrates the need for a Pareto front-like approach to materials discovery for interconnect applications.

2.3 Identification of the most promising interconnect candidates

First, for identifying local, interconnects we consider the following set of surrogate properties: Fermi velocity, density of states at the Fermi level, and reaction energies with O_2, H_2O and SiO_2. We then use a three-stage optimization method to find the best local interconnect candidates. In the first stage, we filter down candidates based on the current state-of-the-art materials. We do so by selecting materials that display an average Fermi velocity $\tilde{v}_F$ higher than Ru, so as to enforce that our desired material has a bulk conductivity at least of the order of that from Ru. For the other properties, including the density of states and the Fermi energy and

reaction energies, we filter down for materials displaying properties at least as good as their corresponding mean. There is an inherent error in utilizing our surrogate properties to approximate desired physical quantities to be optimized. Accordingly, to ensure we do not lose desirable candidates, we add an error bar to our properties prior to constructing a Pareto front, thus obtaining what we denote by a *robust Pareto front*. A material $\mathcal{P}$ on the Pareto front with property $(y_1 \pm \Delta y_1)$ lies on the Pareto front if for every other material $\mathcal{Q}$ with property $y_2 \pm \Delta y_2$ if $y_2 - \Delta y_2 < y_1 + \Delta y_1$. With this, we obtain a list of candidates, though without any particular order. In the final step, we rank the candidates based on a normalized weighted sum of the different properties. We ensure we reward candidates with a holistic property description, instead of displaying a single or few optimal properties, by defining an objective function Z that penalizes materials with unequally optical features,

$$Z(X, w, \alpha) = \sum_i X_i w_i - \alpha \sqrt{(\mathbb{E}(X^2) - \mathbb{E}(X)^2)}, \quad (9)$$

where X is a vector with the features for a given material, w are weights, α is the penalization constant, and $\mathbb{E}$ is the expectation value function.

The end result of our filtering and raking is a list of potential material candidates which meet all desired requirements, and warrant further investigation as potential Cu interconnect alternatives (Figure 3). We also list the identified materials that we expect to outperform Ru, according to our surrogate properties, in Table 2.

For the identification of semi-global interconnects we focus on optimizing two properties: the conductivity and the skin depth of a material. For thickener interconnects, these properties are more critical than the ones discussed in the case of the local interconnects. Ferromagnetic alternatives to laminate stacks will require careful experimental design and study to tune their permeability, and a high conductivity is necessary to ensure a broad range of frequeuncies in which the material can be used. Accordingly, we filter for candidates exhibiting a large volume magnetization ($m > 0.058\ \mu_B/\text{Å}^3$, where μ_B is the Bohr magneton), and no longer include the density of states criterium. We directly rank the top candidates by the surrogate property for conductivity and not by a combination of the surrogate property since the constraint in magnetization reduces the number of materials significantly: only one in roughly 20 candidates from the Materials Project database satisfies this constraint (Figure 4).

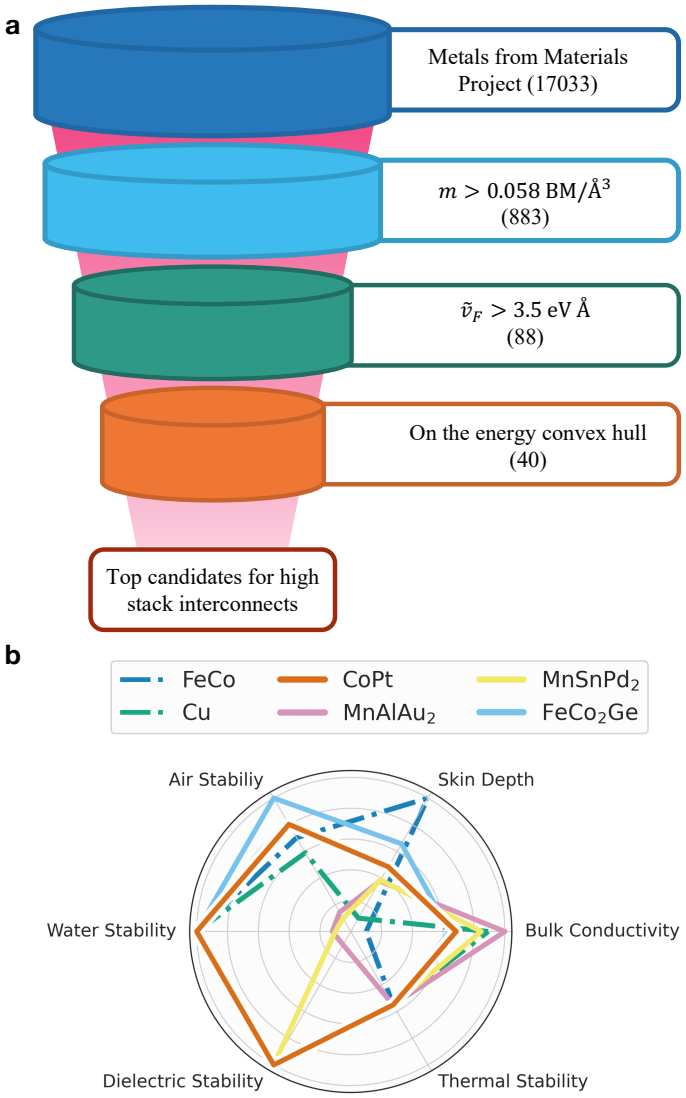

Figure 4: a) Procedure for identification of semi-global interconnects. b) Scaled radar plot, normalized by the maximum value associated with each of the surveyed surrogate properties, for the identified semi-global interconnect candidates from the screening (solid) and the current state-of-the-art alternatives (dotted).

We note from our analysis that there are no materials with simultaneously large surrogates for the bulk magnetization and Fermi velocity, which is supported by the low correlation between these two features (Figure 2). Finally, we select the candidates that lie on the energetic convex hull. Since the relative space consumed by the barrier layer for semi-global interconnects is small, we ignore the reaction surrogates from our screening here as they are not as critical as in the case of local interconnects. We can however visualize these surrogates for our top candidates, allowing for a better selection of materials for future experimental efforts. We show this screening procedure and the comparison between the current state-of-the-art candidates in Figure 4. High saturation magnetization ferromagnets like NiFe and FeCo have been considered as the

ferromagnetic material in laminate stacks. However, these metals also possess lower conductivities. Since our identified metals have higher conductivities they could also be used in these laminate stacks as a potential replacement for FeCo. The identified materials CoPt, $MnAlAu_2$, $FeCo_2Ge$, etc. (Figure 4) can act as potential replacements for both Cu as high stack interconnect and FeCo in laminate stacks.

2.4 Analysis of one of the candidates CoPt: *ab-initio* calculations

With the identification of tens of possible materials for future interconnects applications, we now proceed to validate our approach and, in particular, if our simplified surrogate properties are indeed capable of identifying good interconnect materials that display large bulk conductivity, good scalability (measured by long electron scattering times at surfaces), and stability. We focus our efforts on CoPt, since (1) it is a highly ranked potential interconnect, according to our surrogates; (2) it appears as potential local and semi-global interconnect; (3) its crystal structure is simple enough, with a tetragonal structure with the *P4/mmm* space group (see Figure 5a), that can be studied with higher-level electronic-structure methods; and (4) we can also validate it experimentally, given the previously reported successful synthesis of this compound [41].

We first validate our approach by computing the theoretical limit for the bulk electronic conductivity of CoPt using density-functional theory. The obtained phonon band structure and electronic band structure of CoPt are shown in Figure 5b, c respectively. We obtain the conductivity by solving the iterative Boltzmann transport equation by interpolating electron-phonon coupling matrix elements to highly dense k-, q-point grids (with an up to $100\times100\times100$ sampling for CoPt). After solving this equation, we obtain variation in Fermi velocity and mean free path over the Fermi surface of CoPt. We plot the computed quasiparticle mean-free paths and Fermi velocities in Figure 5.

The synergistic relationship between the high average Fermi velocity, mean free path and carrier density leads to the high conductivity for this system. We compute the relevant resistivity tensor components of CoPt at 300K and obtain $\rho_{xx} = \rho_{yy} = 8.1\ \mu\Omega\,\mathrm{cm}$, and $\rho_{zz} = 8.9\ \mu\Omega\,\mathrm{cm}$. The calculation has been carefully converged to accurately estimate the bulk conductivity of a 6-band Fermi surface. Our computed resistivity of CoPt, $\rho_{\mathrm{CoPt}} \approx 9\ \mu\Omega\,\mathrm{cm}$, compares well against our theoretically computed resistivity for Cu, $\rho_{\mathrm{Cu}} \approx 2.2\ \mu\Omega\,\mathrm{cm}$, using the same methodology, as well as the experimental resistivity for Cu [12], $\rho_{\mathrm{Cu}}^{\mathrm{exp}} \approx 1.8\ \mu\Omega\,\mathrm{cm}$, and Ru [50], $\rho_{\mathrm{Ru}}^{\mathrm{exp}} \approx 7\ \mu\Omega\,\mathrm{cm}$. If, as we predict from our surface scattering time surrogate, CoPt retains its resistivity upon scaling film thickness, then it would be quite an attractive alternative interconnect material, reaching the same performance as Cu for lengths smaller than 10 nm.

2.5 Experimental study of CoPt

As a verification of the calculation methodology, we examine the experimental results of CoPt, which shows excellent conductivity and stability among the predicated materials in Table 2. Figure 6 (a) shows the resistivity of CoPt as a function of thickness, obtained from previous sputtered films [51], in comparison to Ru and Cu with liner data. The Cu with liner, in particular, exhibits a significant increase in resistivity as the thickness decreases due to surface scattering and grain boundary scattering at small dimensions [5]. However, the resistivity of CoPt increases less sharply with decreasing thickness, as predicted by our physically motivated screening methodology. CoPt prepared by sputter deposition and post-growth anneal shows resistivity of 11 $\mu\Omega\,\mathrm{cm}$ at a thickness of 34 nm, and increases to 22 $\mu\Omega\,\mathrm{cm}$ for a film thickness of 7 nm. Based on this trend, CoPt is expected to outperform Cu at smaller length scales, and with further experimental study could outperform Ru at smaller length scales[12, 50].

While these current values are likely still too high for the industry to prefer CoPt over Ru, future improvements in CoPt thin-film quality may change this outlook. Our results also demonstrate that the multiobjective approach described here has identified competitive materials for interconnect applications. Finally, resistivity scaling was not the only surrogate property that was screened for in our methodology. CoPt was predicted to have good air stability compared to other metals [52], which we have confirmed experimentally as shown in Figure 6. The higher experimental resitivity of CoPt makes it not very suitable for application as a ferromagnetic metal interconnect. However, it still remains a candidate as an alternative ferromagnet in the laminate stacks. The higher conductivity metric of the remaining metals make them promising candidates for further experimental study.

Our samples were prepared as follows: we grew a 30 nm thick CoPt film using molecular beam epitaxy (MBE) without post-growth annealing. The film exhibits a single phase and epitaxial growth, as evidenced by streaky reflection high-energy electron diffraction (RHEED) patterns and a single X-ray

Materials Project ID	Chemical formula	Bandstructure Fermi velocity (eV Å)	O_2 reaction energy (eV / O_2)	H_2O reaction energy (eV / H_2O)	SiO_2 reaction energy (eV / SiO_2)	Density of states (States/(eVÅ^3))	Objective value Z
mp-945	NiPt [39]	4.9	-2.8	0.0	0.0	0.11	2.89
mp-12798	Ni_3Pt [40]	4.1	-1.8	0.0	0.0	0.15	2.78
mp-949	CoPt [41]	5.4	-2.9	0.0	0.0	0.08	2.40
mp-1193415	Cd_8Au_5 [42]	5.2	-1.4	0.0	0.0	0.05	2.10
mp-1008349	Co_3Ni [43]	4.2	-1.9	0.0	0.0	0.11	1.64
mp-22300	$FeCo_2Ge$ [44]	5.1	-2.5	0.0	0.0	0.06	1.57
mp-922	$CoPt_3$ [45]	4.1	-1.6	0.0	0.0	0.10	1.27
mp-3702	$FeCuPt_2$ [46]	4.6	-2.5	0.0	0.0	0.06	0.80
mp-1918	FeRh [47]	4.5	-3.1	0.0	0.0	0.08	0.78
mp-22320	GaRu [48]	5.2	-4.2	0.0	0.0	0.07	0.76
mp-33	*Ru*	*4.7*	*-2.9*	*0.0*	*0.0*	*0.06*	*0.61*

Table 2: List of the 10 most promising local interconnect candidates with a higher objective value than Ru identified from this work , with their relevant surrogate properties. The references cited point to the corresponding ICSD article with their synthesis details.

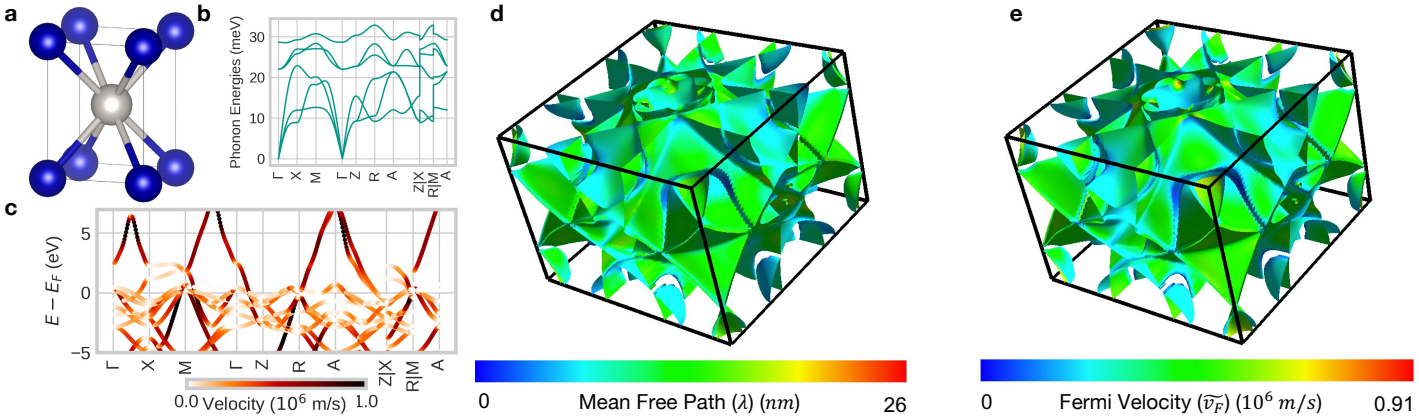

Figure 5: a) Crystal structure of CoPt. b) Interpolated phonon bands of CoPt. c) Interpolated band structure of CoPt, coloured by the magnitude of their wannier interpolated velocities. d) Variation of mean free path across the Fermi surface of CoPt, and e) Variation of Fermi velocity across the Fermi surface of CoPt [49].

diffraction (XRD) peak (see Figure 6). We also hope that future work on these materials can improve the observed resistivity, and film quality, and utilize growth conditions that are back-end-of-the-line compatible. In particular, the resistivity exhibits no change even after 213 days of exposure to air at 294 K and 49% humidity, compared to that of as-grown CoPt measured on day 1. X-ray photoelectron spectroscopy (XPS) was also performed in order to further study surface oxidation. The inset of Figure 4b shows a comparison of the XPS of in-situ measurement on the as-grown sample (day 1) and the same sample after air exposure for 213 days. The line shape of both the Pt 4f and the Co 2p regions are more stable than Cu over that timeframe, indicating only minor chemical changes in addition to the reduction in signal-to-noise ratio due to physisorbed surface species. Altogether, these results show that CoPt has excellent oxidation resistance as predicted in our screening efforts.

3 Conclusion

In this paper, we demonstrated a rapid, multi-objective screening method to identify interconnect materials to replace Cu. Our method highlights the need to optimize for property tradeoffs to evaluate materials holistically for a particular application. This allows us to identify multiple replacements for Cu for local interconnects and high-frequency applications. Our *ab-initio* studies on CoPt, one of the identified materials quantitatively support the performance of these the surrogate for bulk conducitvity and validate our screening methods for high-performing materials. In addition, we experimentally validated our predictions and demonstrated the potential experimental viability of one of the identified interconnect materials, CoPt, which features extremely promising air stability results from this work, and promising resistivity value in the sputtered 6-10 nm range from the literature. This highlights its potential to

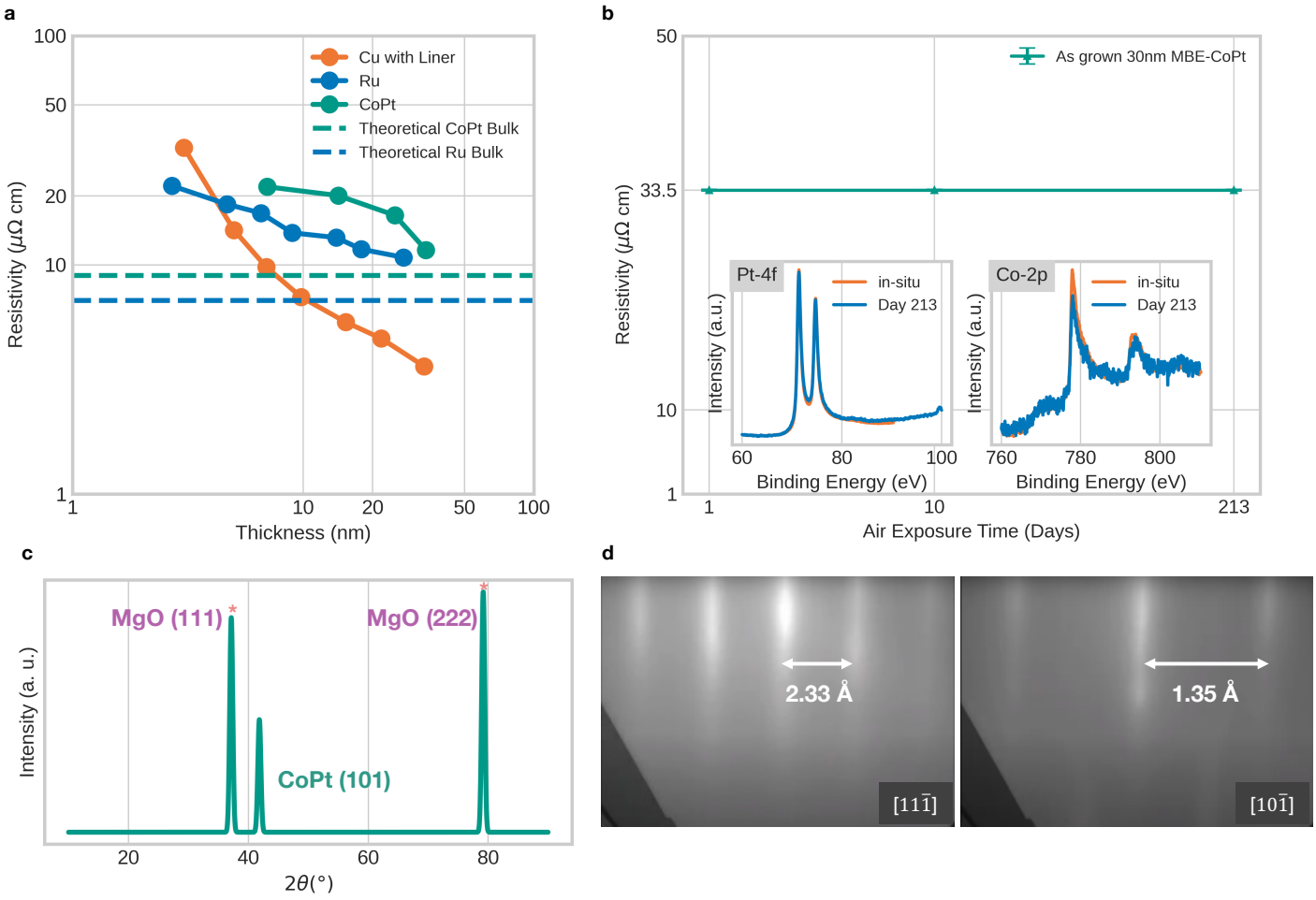

Figure 6: a) Thickness-dependent resistivity of sputtered CoPt [51], Ru [12], and Cu [12] with liner. CoPt shows a smaller increase in resistivity as the thickness decreases compared to Cu with liner. The solid lines shown in the plot are a guide to the eyes, connecting the points, not a physical resistivity trend b) Resistivity evolution upon air exposure of a 30 nm thick CoPt film grown by MBE, showing no resistivity change after air exposure over hundreds of days. Inset is the comparison of the XPS spectra of in-situ as-grown CoPt and the same CoPt after being exposed to air for 213 days. The line shape of Pt 4f and Co 2p regions have very minimal change over time indicating an oxidation-resistant film as predicted. c) Bragg-Brentano XRD of 30 nm CoPt on MgO (111) shows a single diffraction peak of CoPt (101) (primitive cell), indicating a pure phase of CoPt. Stars mark the peaks from the MgO substrate. d) RHEED patterns of 30 nm CoPt on MgO (111) in [11$\bar{1}$]and [10$\bar{1}$] directions show different spacing between streaks, indicating epitaxial growth.

surpass Cu at thicknesses below ~ 5 nm.. Given these exciting preimilary results, we look forward to future experimental works both improving the growth process and contact engineering of CoPt thin films, and also validating other interconnect materials identified in this work.

4 Experimental Details and Theoretical Methods

4.1 Dataset of metrics and optimization steps

The metrics were computed from metal data pulled from the Materials Project database in 2021. We share the computed metrics here: Github and an easy to use Google Colab interface. Using this interface, one can change various parameters of the screening process and find candidates suited to their desired criteria.

4.2 *Ab-inito* calculations

We perform *ab-initio* DFT and DFPT calculations using Quantum ESPRESSO [53] with an energy cutoff of 100 Ry and on a uniform $12\times12\times8$ k-point grid for the self-consistent-field calculation. We use scalar relativistic potentials [54]. We perform the DFPT calculations on a set of $3\times3\times2$ phonon momenta (q-point grid). We then use the Perturbo code [55] to perform an iterative Boltzmann transport approximation calculation for the conductivity. The com-

puted electron-phonon coupling elements are interpolated onto 100×100×100 k- and q-point grids. We interpolate the electron-phonon matrix elements using the Wannier90 code [35], using an automated approach based on the selected column of the density matrix (SCDM-k) for the initial projection [56, 57].

4.3 Experimental growth and analysis

The MBE growth of CoPt was carried out in a ScientaOmicron Materials Innovation Platform (MIP) integrated with MBE, ALD, and XPS. MgO (111) was used as the substrate, and Co and Pt evaporation was carried out using a regular Knudsen cell and an e-beam evaporator, respectively. The growth temperature was 750 °C and the thickness was calibrated by an in-situ film thickness monitor and confirmed by cross-sectional transmission electron microscopy. XPS was carried out using a monochromated Al X-ray source ($h\nu$ = 1486.7 eV) and Argus CU analyzer. Resistivities were measured using an HL5500PC Hall effect measurement system in a van der Pauw configuration. XRD was performed using a Panalytical Aeris system.

4.4 Statistical Analysis

The complete data is available here. In the plots of Figures 3 and 4 the data was normalized to be in the range of [0,1] for visual clarity. The filtering and Pareto front step are performed without any data processing. When we compute the objective function, we normalize the given objectives by their mean and standard deviation to ensure appropriate relative weighting. The measurements in Fig 5, are from one sample. All data analysis, and filtering code was written in python using the following packages for statistical analysis: numpy, scipy, sklearn.

Acknowledgements

This project was supported by the Semiconductor Research Corporation (SRC) nCore IMPACT Centre (Task 2966.001), the National Science Foundation (NSF) program Designing Materials to Revolutionize and Engineer our Future (DMREF) via a project DMR-1922312, and SUPREME, one of seven centers in JUMP 2.0, an SRC program sponsored by DARPA. GZ, PL, YL, CLH acknowledge the funding from SRC nCore's IMPACT Centre (Task 2966.004). We would like to thank Dr. Harsono Simka for discussions on the importance of the stability surrogate properties, Prof. Peter Asbeck and Prof. Eric Fullerton for discussion on skin depth, Prof. Ravishankar Sundararaman, Prof. Judy Cha, Prof. Daniel Gall for general interconnect technologies, and Dr. Jonah Haber for discussions on conductivity calculations. We would also like to thank Drs. Chris Ciccarino and Brandi Ransom for their comments on the initial drafts of this manuscript. This research used resources of the National Energy Research Scientific Computing Center (NERSC), a U.S. Department of Energy Office of Science User Facility located at Lawrence Berkeley National Laboratory, operated under Contract No. DE-AC02-05CH11231 using NERSC award BES-ERCAP ERCAP0024305 to perform the surrogate property computation and screening of the candidate materials. Calculations of the CoPt electronic conductivity used computational resources from the Texas Advanced Computing Center (TACC) at The University of Texas at Austin, funded by the National Science Foundation (NSF) award 1818253, through allocation DMR21077.

Conflict of Interest

The authors declare no conflict of interest.

Author Contributions

AR performed the multi-objective screening and DFT calculations on CoPt with the help of ERA. AR, EJR and FHJ formulated the surrogate properties. AR, GZ, CLH, and FHJ wrote the manuscript. GZ, YL, PL grew the MBE CoPt samples and GZ, PL performed the material and electronic characterization of the CoPt films. CLH supervised the experimental work, FHJ supervised the screening and theoretical calculations.

References

[1] IRDS, *IRDS* **2021**, publisher: IEEE.

[2] A. F. Mayadas, M. Shatzkes, *Phys. Rev. B* **1970**, *1*, 4 1382, publisher: American Physical Society.

[3] E. Sondheimer, *Advances in Physics* **1952**, *1*, 1 1, publisher: Taylor & Francis.

[4] S. Kumar, C. Multunas, B. Defay, D. Gall, R. Sundararaman, *Phys. Rev. Materials* **2022**, *6*, 8 085002, arXiv:2204.13458 [cond-mat, physics:physics].

[5] D. Gall, J. J. Cha, Z. Chen, H.-J. Han, C. Hinkle, J. A. Robinson, R. Sundararaman, R. Torsi, *MRS Bulletin* **2021**, *46*, 10 959.

[6] K. Sankaran, K. Moors, Z. Tőkei, C. Adelmann, G. Pourtois, *Phys. Rev. Materials* **2021**, *5*, 5 056002.

[7] S. Kumar, Y.-H. Tu, L. Sheng, N. A. Lanzillo, T.-R. Chang, G. Liang, R. Sundararaman, H. Lin, C.-T. Chen, Anomalous conductance scaling in Weyl semimetal NbAs, **2022**, URL `http://arxiv.org/abs/2211.10426`, ArXiv:2211.10426 [cond-mat].

[8] Y. Zhu, D. A. Rehn, E. R. Antoniuk, G. Cheon, R. Freitas, A. Krishnapriyan, E. J. Reed, *ACS Nano* **2021**, *15*, 6 9851, publisher: American Chemical Society.

[9] C. Zhang, Z. Ni, J. Zhang, X. Yuan, Y. Liu, Y. Zou, Z. Liao, Y. Du, A. Narayan, H. Zhang, et al., *Nature materials* **2019**, *18*, 5 482.

[10] H. J. Han, S. Kumar, X. Ji, J. L. Hart, G. Jin, D. J. Hynek, Q. P. Sam, V. Hasse, C. Felser, D. G. Cahill, R. Sundararaman, J. J. Cha, Topological Metal MoP Nanowire for Interconnect, **2022**, URL `http://arxiv.org/abs/2208.02784`, ArXiv:2208.02784 [cond-mat].

[11] D. Gall, *Journal of Applied Physics* **2020**, *127*, 5 050901.

[12] S. Dutta, K. Sankaran, K. Moors, G. Pourtois, S. Van Elshocht, J. Bömmels, W. Vandervorst, Z. Tőkei, C. Adelmann, *Journal of Applied Physics* **2017**, *122*, 2 025107.

[13] C. Ting, In *1984 International Electron Devices Meeting*. **1984** 110–113.

[14] J. Koike, T. Kuge, L. Chen, M. Yahagi, In *2021 IEEE International Interconnect Technology Conference (IITC)*. **2021** 1–3, ISSN: 2380-6338.

[15] J.-P. Soulié, Z. Tőkei, J. Swerts, C. Adelmann, In *2021 IEEE International Interconnect Technology Conference (IITC)*. **2021** 1–3, ISSN: 2380-6338.

[16] J.-P. Soulié, Z. Tőkei, J. Swerts, C. Adelmann, In *2022 IEEE International Interconnect Technology Conference (IITC)*. **2022** 73–75, ISSN: 2380-6338.

[17] H. Li, C. Xu, N. Srivastava, K. Banerjee, *IEEE Transactions on Electron Devices* **2009**, *56*, 9 1799, conference Name: IEEE Transactions on Electron Devices.

[18] C.-L. Lo, M. Catalano, A. Khosravi, W. Ge, Y. Ji, D. Y. Zemlyanov, L. Wang, R. Addou, Y. Liu, R. M. Wallace, et al., *Advanced Materials* **2019**, *31*, 30 1902397.

[19] L. Chen, S. Kumar, M. Yahagi, D. Ando, Y. Sutou, D. Gall, R. Sundararaman, J. Koike, *Journal of Applied Physics* **2021**, *129*, 3 035301.

[20] M. Zhang, S. Kumar, R. Sundararaman, D. Gall, *Journal of Applied Physics* **2023**, *133*, 4 045102.

[21] A. Rahimi, Y.-K. Y. Yoon, In *2014 IEEE 64th Electronic Components and Technology Conference (ECTC)*. **2014** 736–741, ISSN: 2377-5726.

[22] H. Yamada, *Engineering Research Express* **2023**, *5*, 1 015079.

[23] M. Ashby, *Acta materialia* **2000**, *48*, 1 359.

[24] P. Zhang, Y. Qian, Q. Qian, *Materials Today Communications* **2021**, *28* 102709.

[25] A. M. Gopakumar, P. V. Balachandran, D. Xue, J. E. Gubernatis, T. Lookman, *Scientific reports* **2018**, *8*, 1 3738.

[26] R. Arróyave, D. Khatamsaz, B. Vela, R. Couperthwaite, A. Molkeri, P. Singh, D. D. Johnson, X. Qian, A. Srivastava, D. Allaire, *MRS Communications* **2022**, 1–13.

[27] A. Solomou, G. Zhao, S. Boluki, J. K. Joy, X. Qian, I. Karaman, R. Arróyave, D. C. Lagoudas, *Materials & Design* **2018**, *160* 810.

[28] B. Ransom, N. Zhao, A. D. Sendek, E. D. Cubuk, W. Chueh, E. J. Reed, *MRS Bulletin* **2021**, *46*, 12 1116.

[29] A. Jain, S. P. Ong, G. Hautier, W. Chen, W. D. Richards, S. Dacek, S. Cholia, D. Gunter, D. Skinner, G. Ceder, K. A. Persson, *APL Materials* **2013**, *1*, 1 011002, publisher: American Institute of Physics.

[30] J. M. Munro, K. Latimer, M. K. Horton, S. Dwaraknath, K. A. Persson, *npj Comput Mater* **2020**, *6*, 1 1, number: 1 Publisher: Nature Publishing Group.

[31] D. Zagorac, H. Müller, S. Ruehl, J. Zagorac, S. Rehme, *J Appl Cryst* **2019**, *52*, 5 918, number: 5 Publisher: International Union of Crystallography.

[32] A. Jain, G. Hautier, S. P. Ong, C. J. Moore, C. C. Fischer, K. A. Persson, G. Ceder, *Phys. Rev. B* **2011**, *84*, 4 045115, publisher: American Physical Society.

[33] H. Lee, S. Poncé, K. Bushick, S. Hajinazar, J. Lafuente-Bartolome, J. Leveillee, C. Lian, F. Macheda, H. Paudyal, W. H. Sio, et al., *arXiv preprint arXiv:2302.08085* **2023**.

[34] G. K. Madsen, D. J. Singh, *Computer Physics Communications* **2006**, *175*, 1 67.

[35] G. Pizzi, V. Vitale, R. Arita, S. Blügel, F. Freimuth, G. Géranton, M. Gibertini, D. Gresch, C. Johnson, T. Koretsune, et al., *Journal of Physics: Condensed Matter* **2020**, *32*, 16 165902.

[36] T. Morikawa, Y. Nishibe, H. Yamadera, Y. Nonomura, M. Takeuchi, Y. Taga, *IEEE Transactions on Magnetics* **1997**, *33*, 5 4367.

[37] M. Yamaguchi, Y. Endo, N. Sato, A. Ludwig, In *2011 6th European Microwave Integrated Circuit Conference*. IEEE, **2011** 77–80.

[38] S. P. Ong, L. Wang, B. Kang, G. Ceder, *Chem. Mater.* **2008**, *20*, 5 1798, publisher: American Chemical Society.

[39] U. Esch, A. Schneider, *Zeitschrift für Elektrochemie und angewandte physikalische Chemie* **1944**, *50*, 11-12 268.

[40] A. Kussmann, H. Vonsteinwehr, *Zeitschrift fur Metallkunde* **1949**, *40*, 7 263.

[41] J. Woolley, J. Phillips, J. Clark, *Journal of the Less Common Metals* **1964**, *6*, 6 461.

[42] K. Alasafi, K. Schubert, *Journal of the Less Common Metals* **1979**, *65*, 1 P23.

[43] T. Omori, K. Oikawa, J. Sato, I. Ohnuma, U. R. Kattner, R. Kainuma, K. Ishida, *Intermetallics* **2013**, *32* 274.

[44] K. V. Buschow, P. Van Engen, R. Jongebreur, *Journal of magnetism and magnetic materials* **1983**, *38*, 1 1.

[45] S. Jen, *Journal of alloys and compounds* **1996**, *234*, 2 231.

[46] M. Shahmiri, D. Vaughan, S. Murphy, *physica status solidi (a)* **1986**, *95*, 1 63.

[47] S. A. Makhlouf, T. Nakamura, M. Shiga, *Journal of magnetism and magnetic materials* **1994**, *135*, 3 257.

[48] W. Jeitschko, H. Holleck, H. Nowotny, F. Benesovsky, *Monatshefte für Chemie und verwandte Teile anderer Wissenschaften* **1963**, *94* 838.

[49] M. Kawamura, *Computer Physics Communications* **2019**, *239* 197.

[50] M. Breeden, V. Wang, R. Kanjolia, M. Moinpour, J. Woodruff, H. Simka, A. Kummel, In *2022 IEEE International Interconnect Technology Conference (IITC)*. IEEE, **2022** 120–122.

[51] S. Kundu, R. Roy, M. S. Rahman, S. Upadhyay, R. O. Topaloglu, S. E. Mohney, S. Huang, S. Ghosh, *Journal of Low Power Electronics and Applications* **2023**, *13*, 1 16.

[52] S. Sharma, L. Hines, *IEEE Transactions on Components, Hybrids, and Manufacturing Technology* **1983**, *6*, 1 89.

[53] P. Giannozzi, S. Baroni, N. Bonini, M. Calandra, R. Car, C. Cavazzoni, D. Ceresoli, G. L. Chiarotti, M. Cococcioni, I. Dabo, A. D. Corso, S. d. Gironcoli, S. Fabris, G. Fratesi, R. Gebauer, U. Gerstmann, C. Gougoussis, A. Kokalj, M. Lazzeri, L. Martin-Samos, N. Marzari, F. Mauri, R. Mazzarello, S. Paolini, A. Pasquarello, L. Paulatto, C. Sbraccia, S. Scandolo, G. Sclauzero, A. P. Seitsonen, A. Smogunov, P. Umari, R. M. Wentzcovitch, *J. Phys.: Condens. Matter* **2009**, *21*, 39 395502.

[54] M. J. van Setten, M. Giantomassi, E. Bousquet, M. J. Verstraete, D. R. Hamann, X. Gonze, G.-M. Rignanese, *Computer Physics Communications* **2018**, *226* 39.

[55] J.-J. Zhou, J. Park, I.-T. Lu, I. Maliyov, X. Tong, M. Bernardi, *Computer Physics Communications* **2021**, *264* 107970.

[56] V. Vitale, G. Pizzi, A. Marrazzo, J. R. Yates, N. Marzari, A. A. Mostofi, *npj Comput Mater* **2020**, *6*, 1 1, number: 1 Publisher: Nature Publishing Group.

[57] A. Damle, L. Lin, L. Ying, *Journal of Computational Physics* **2017**, *334* 1.